Synergistic effect of the co-solvent induced interfacial chemistries in aqueous Zn batteries

Chen Hu [a,b], Gaoli Guo [a], Huihua Li [c], Jian Wang [d,e], Zhengqing Liu [a], Leilei Zheng [a], Huang Zhang [a,b,c,*]

[a] Institute of Flexible Electronics, Northwestern Polytechnical University, Xi'an 710072, China
[b] Chongqing Innovation Center, Northwestern Polytechnical University, Chongqing 401135, China
[c] Key Laboratory of Engineering Dielectric and Applications (Ministry of Education), School of Electrical and Electronic Engineering, Harbin University of Science and Technology, Harbin 150080, China
[d] Helmholtz Institute Ulm (HIU), Helmholtzstrasse 11, Ulm D-89081, Germany
[e] Karlsruhe Institute of Technology (KIT), P.O. Box 3640, Karlsruhe D-76021, Germany

Keywords:
Aqueous electrolyte
Zn anode
Interfacial chemistry
Solvation structure
Reversibility

A B S T R A C T

Aqueous zinc-ion batteries (ZIBs) have garnered significant attention due to their high energy, intrinsic safety, and environmental friendliness. NASICON-type compounds are promising cathode candidates in aqueous batteries due to their high ionic conductivity, and high operating voltage. However, these materials, e.g., $Na_3V_2(PO_4)_3$, suffer from inevitable structural degradation and dissolution in aqueous electrolytes, thus hampering their practical performance in aqueous batteries. Interfacial chemistry modulation by electrolyte engineering is beneficial for stabilizing Zn metal anode and high-voltage cathodes in ZIBs. Herein, the interfacial chemistries in an engineered non-concentrated aqueous electrolyte by co-solvent strategy are reported, which synergistically enables high reversibility of Zn anode and long cycling stability of $Na_3V_2(PO_4)_3$ cathode. Consequently, the Zn||$Na_3V_2(PO_4)_3$ full-cell exhibits high Coulombic efficiency (~99.3% in average) with a prolonged cycling life, which can be ascribed to the synergistic-effect of the solid-electrolyte interphases with unique organic/inorganic hybrid structures on the electrodes. This work discloses the structures of the interphases formed on the electrodes induced by co-solvent strategy in aqueous electrolytes and their working mechanisms in stabilizing the aqueous Zn batteries, which will guide the future design of advanced aqueous electrolytes with unique interfacial chemistries for batteries.

1. Introduction

The depletion of fossil fuels along with the resulting global environmental problems have forced to the emerging energy transition to low-carbon sources of electricity, while developing reliable, safe and high efficiency electrochemical energy storage technologies are still challenging for their utilization [1,2]. Aqueous zinc ion batteries (ZIBs) have been regarded as one of the most promising candidates for grid-scale energy storage due to their high energy, low cost, intrinsic safety and high material sustainability [3]. However, their practical implementations and further development are restricted by numerous urgent issues including but not limited to degradation of the cathode, inferior reversibility of zinc anode and the inevitable occurrence of side reactions [4]. To build more advanced batteries, extensive efforts have been devoted to improving the overall performance of ZIBs, such as exploring cathode materials with high capacity [5], electrolyte engineering [6], achieving metallic zinc anode with high reversibility [7], and building artificial interphases to protect the electrodes [8,9].

To date, great achievements have been made to search for promising cathode materials with regard to reversible Zn storage, including vanadium-based oxides [10], manganese-based oxides [11], Prussian blue analogues [12], and organic compounds [13]. Although metal oxide-based cathodes exhibit high theoretical capacities, they always suffer from fast capacity fading arising from the dissolution of metal ions [14,15]. Prussian blue analogues usually display limited capacity of less than 100 mAh g^{-1} [16]. However, these materials also exhibit unsatisfactory performance such as low operating voltage and structural instability during charge/discharge process in aqueous media [17]. The

* Corresponding author.
E-mail address: iamhzhang@nwpu.edu.cn (H. Zhang).

sodium superionic conductor (NASICON)-structured compounds in a general formula of $A_xMM'(XO_4)_3$ (A = Li, Na, K; M or M′ = Fe, V, Ti, Cr, Mn; X = S, P, Si, As) with robust open three-dimensional (3D) framework are gaining rapid attention as promising cathode materials for batteries owing to their fast ion conduction and thermal stability [18]. Besides, the inducing effect of polyanion units (e.g., $(PO_4)_3$) in the framework can lead to higher redox voltage and more vacancies to store metal ions, thus contributing to the high energy density and safety [19,20]. As a typical example of NASICION compounds, the $Na_3V_2(PO_4)_3$ (NVP) material has been found to be capable of simultaneous (de) intercalation by Zn^{2+}/Na^+ ions in the Zn-based aqueous electrolytes [21,22]. Even though, these polyanionic materials often demonstrate inferior cycling properties in aqueous electrolytes like capacity fading over prolonged cycling due to the structural collapse and degradation accompany with material dissolution, which will reduce the utilization of active materials and induce severe efficiency decay [23,24].

In this regard, constructing solid-electrolyte interphases (SEI), including cathode-electrolyte interphase (CEI) and anode-electrolyte interphase (AEI), on the electrodes and reduce the content of active water by electrolyte regulation can be efficient strategies to protect the electrodes and improve the long cycling stability for ZIBs [25]. In our previous work, it has been reported that the electrolyte manipulation in aqueous electrolyte can facilitate the SEI formation on the NVP cathode, thus improving the reversibility of Zn-NVP aqueous batteries [26]. However, the synergistic effect of the electrolyte regulation on both the anode and cathode was not detailedly investigated. Particularly, the efforts on electrolyte regulation have been proven efficiently in improving the reversibility of Zn anode, in which the co-solvent strategy attracts particular interest [27,28]. For example, the introduction of 1, 2-dimethoxyethane (DME) additive into a dilute zinc trifluoromethanesulfonate ($Zn(OTF)_2$) aqueous electrolyte significantly improved the reversibility of Zn anode, which can be attributed to the suppressed water-reactivity, and in-situ formation of an organic-inorganic hybrid ZnF_2-ZnS-rich interphase on Zn surface [29]. Moreover, a water/propylene carbonate (PC) mixture hybrid electrolyte was also proved to be efficient to stabilize the Zn anode and enable an anode-free aqueous Zn battery [30]. However, the interfacial chemistries of co-solvent strategy and the specific interphase structures on the specific cathode and anode remain yet to be explored, which are especially critical for the rational design of advanced aqueous electrolytes and interphases for AZBs.

Herein, we synergistically investigate the unique interfacial chemistries of co-solvent strategy in the $Zn(OTF)_2$-based aqueous electrolyte for aqueous ZIBs. The tetraethylene glycol dimethyl ether (TEGDME) was selected as the example, which has unlimited mutual solubility in water and holds great potential in constructing H-bonds with H_2O. It is proven that the addition of TEGDME successfully reduces the reactivity of water and alleviates the hydrogen evolution reaction (HER), thereby enabling the high reversibility of Zn anode (over 4500 h at 0.5 mA cm $^{-2}$ with 0.5 mAh cm $^{-2}$) and improved structural stability of NVP cathode upon long-term cycling. Interestingly, postmortem XPS results indicate the existence of quite distinct solid-electrolyte interphases on the positive and negative electrodes, considering mainly due to the catalytic action of vanadium dissolution, which contributes to the formation of a robust CEI on the cathode side. This work evidences the co-solvent induced solid-electrolyte interphases for stabilizing the Zn anode and NVP cathode in aqueous electrolytes, and provides basic understandings and prospects on the structure of interphases in stabilizing the electrodes, which can guide the future electrolyte design with unique interfacial chemistries for aqueous batteries.

2. Experimental section

2.1. Material synthesis

The NASICON-type $Na_3V_2(PO_4)_3$ compounds were synthesized by a typical solid-state method. Specifically, $CH_3COONa{\cdot}3H_2O$ (99%, VWR), NH_4VO_3 (99%, Sigma-Aldrich), and $NH_4H_2PO_4$ (99%, Alfa) (molar ratio: 3:2:4) were dissolved in an aqueous citric acid ($C_6H_8O_7{\cdot}H_2O$, 99%, Alfa) solution and then dried at 80 °C in a hot air cabinet. The precursors were grounded and pre-heated at 350 °C for 6 h, then calcined at 800 °C for 12 h under Ar flow. The final products were collected and grounded for further use.

2.2. Electrolyte preparation

The aqueous electrolytes were prepared by dissolving specific salts in Milli-Q water while tetraethylene glycol dimethyl ether (TEGDME, 99%, Aladdin) was as co-solvent additive. Specifically, 2 mol kg $^{-1}$ Zn $(CF_3SO_3)_2$ ($Zn(OTF)_2$, >99%, Adamas) was added in Milli-Q water, and the solution was denoted as 2mZn. For the co-solvent system, 25 wt.% of TEGDME to the water weight was added into the 2mZn system and denoted as 2mZn-TEGDME. Before use, the electrolytes were degassed with N_2 for 30 min to remove the dissolved O_2.

2.3. Material characterizations

X-ray diffraction (XRD) results were collected on a Bruker D8 Advance diffractometer (Cu Kα = 0.154 nm). The morphologies of the materials and electrodes were characterized by field emission scanning electron microscopy (FE-SEM, Gemini 300). X-ray photoelectron spectroscopy (XPS, PHI 5000 Versa Probe III) was used to analyses the chemical compositions on the surface of cycled electrodes. Ar^+ sputtering was used to understand the chemical compositions in the depth. All the binding energies were calibrated by using the C1s peak (284.8 eV) as reference. Fourier Transform Infrared spectroscopy (FT-IR) was performed on Bruker Tensor II to investigate the properties of water in electrolytes. Raman spectra were collected on a Bruker Vertex70 FTIR spectrometer in RAM II FT Raman module with a laser wavelength of 1064 nm for 1000 scans and a resolution of 2 cm $^{-1}$. The spectra were further analyzed using PeakFit software (v4.12, Sea-Solve Software. Inc.). Electrodes from the disassembled cells were rinsed with water and ethanol, and vacuum dried for the ex-situ measurements. The contact angles of the as-prepared electrolytes on Zn foil were tested by Kruss DSA100 with 2 μL electrolyte.

2.4. Electrochemical characterizations

The cathodes were fabricated by pressing a slurry containing 80 wt.% active materials ($Na_3V_2(PO_4)_3$ (NVP)), 10 wt.% conductive carbon (Super C65, IMERYS), and 10 wt.% polyvinylidene fluoride (PVDF, Solef 6020, Solvay) in N-methyl-2-pyrrolidone (NMP, $H_2O \leq 50$ ppm, 99.5%, Innochem) on a stainless foil (type-316, thickness: 0.02 mm, Ø 12 mm). After drying at 80 °C in air and further drying under vacuum at 120 °C for 12 h, the electrodes were stored in dry-room for further use as cathodes. The Zn reversibility was tested in CR2032 coin-type cells using Zn discs (30 μm, purity: 99.95+%, Ø16 mm) as counter electrodes, glass fiber discs (GF/D, Whatman, Ø 18 mm) as separators, either Cu discs or Zn discs as working electrodes. The full cells were fabricated using NVP cathodes, glass fiber separators and Zn discs ad anodes. The stripping-plating and galvanostatic charge-discharge (GCD) tests of the cells were performed on a battery tester (CT-4000, NEWARE). The mass loading of active materials in cathode was approximately 2.0 mg cm $^{-2}$. The electrochemical workstation (CHI 660E) was used for the cyclic voltammetry (CV), electrochemical impedance spectroscopy (EIS) and linear sweep voltammetry (LSV) measurements. LSV tests of Zn||stainless steel cells were carried out at a sweeping rate of 10 mV s $^{-1}$. EIS results were recorded on the fresh cells and cycled cells at discharged state, with a signal amplitude of 10 mV over the frequency range from 100 kHz to 100 mHz. The ionic conductivity (σ) can be calculated by the following equation:

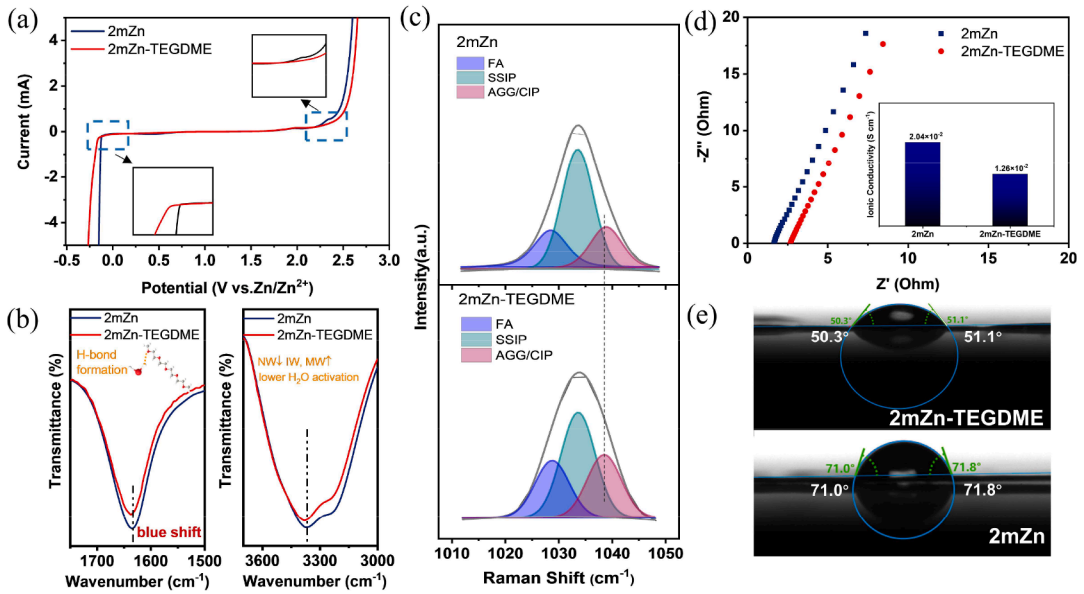

Fig. 1. Characterizations of the aqueous electrolytes. (a) Electrochemical stability windows of the 2mZn and 2mZm-TEGDME electrolytes. (b) FTIR spectra of H—O bending and H—O stretching for the electrolytes. (c) Raman spectra in the wavenumber region of SO_3 stretching modes. FA: free anions; SSIP: solvent separated ion pairs; AGG: aggregations; CIP: contact ion pairs. (d) AC impedance curves of the two electrolytes and the corresponding ionic conductivities in the inset image; (e) Contact angle measurements of the electrolytes on Zn anode.

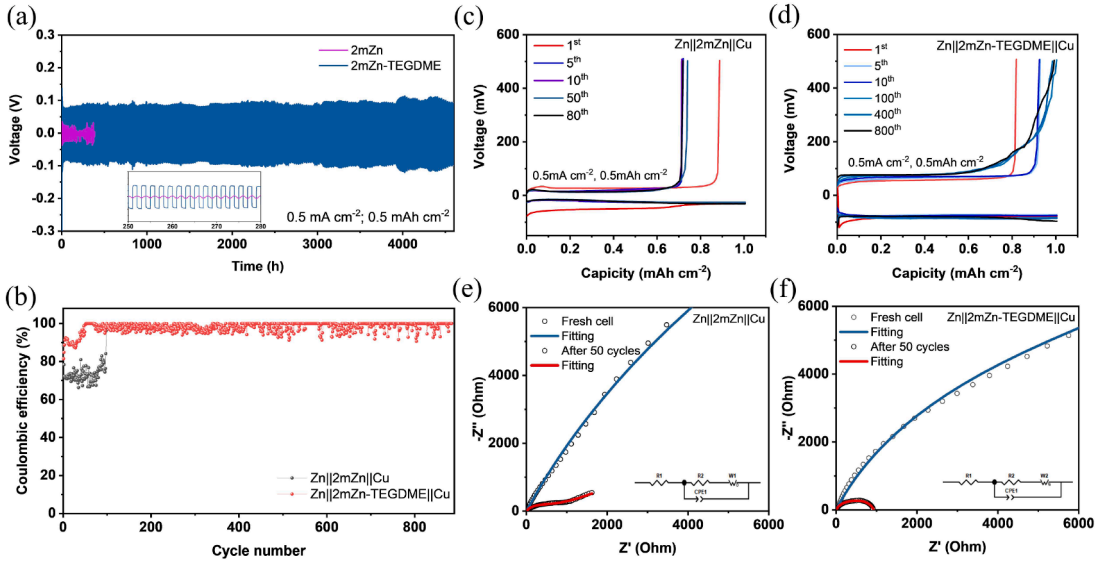

Fig. 2. Electrochemical performance of Zn electrode. (a) Galvanostatic cycling stability of symmetric Zn||Zn cells under 0.5 mA cm^{-2}. (b) CEs of asymmetric Zn||Cu cells at 0.5 mA cm^{-2}. Typical voltage profiles of Zn||Cu cells in (c) 2mZn and (d) 2mZn-TEGDME electrolytes. Nyquist plots of asymmetric Zn||Cu cells in (e) 2mZn; (f) 2mZn-TEGDME electrolytes.

$$\sigma = \frac{L}{R_b S}$$

where R_b represents the electrolyte resistance which can be calculated from EIS tests, L represents the thickness of electrolyte (namely the thickness of separator after package, 675 μm), and S is the contact area between electrode and electrolyte in the testing cell (2.01 cm^{2}). The amount of the electrolyte used for all the cells was fixed in120μl for each cell.

3. Results and discussion

To investigate the effect of co-solvent in the aqueous electrolyte, two electrolytes were prepared, namely 2 m $Zn(OTF)_2$ (m: mol kg^{-1}) and 2 m $Zn(OTF)_2$ in water/TEGDME (4:1 by weight) (hereafter denoted as 2mZn and 2mZn-TEGDME). Fig. 1 presents the electrochemical stability of the two electrolytes. The 2mZn electrolyte exhibit an electrochemical stability window (ESW) of ~2.1 V, while the ESW of 2mZn-TEGDME electrolyte broadens to about 2.4 V [31]. Furthermore, the hydrogen evolution reaction (HER) and oxygen evolution reaction (OER) behaviors of these electrolytes were also analyzed as shown in the insets. Due to the added TEGDME, the hydrogen-bond network of water was changed and the Zn^{2+}-solvation structure was regulated by the co-participation of TEGDME molecules and OTF anions, indicating that the addition of TEGDME can efficiently weaken the water reactivity, and be beneficial to the suppression of water-involved side-reactions [29,

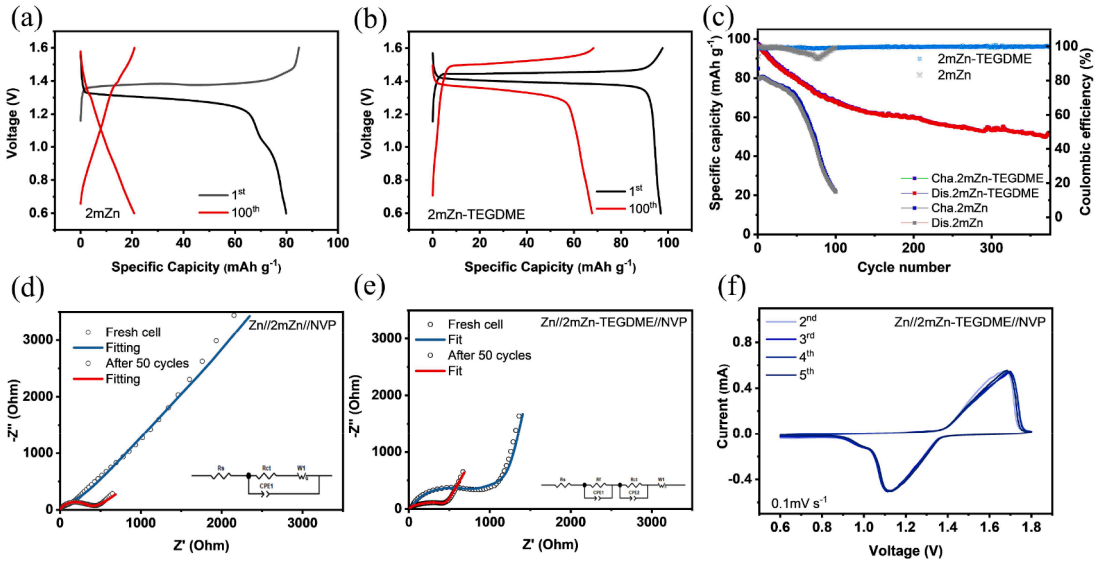

Fig. 3. Electrochemical performance of Zn||NVP full cells. GCD profiles at the 1st and 100th cycles in (a) 2mZn and (b) 2mZn-TEGDME electrolytes. (c) Long-term cycling performance of Zn||NVP cells. Nyquist plots of full cells in (d) 2mZn and (e) 2mZn-TEGDME electrolytes. (f) Cyclic voltammograms (CV) curves for the Zn||NVP full cell in the 2mZn-TEGDME electrolyte at a scan rate of 0.1 mV s^{-1}. All the tests were performed at 50 mA g^{-1} in the voltage range of 0.6–1.6 V. Specific capacity was calculated based on the cathode mass.

32].

The electrolytes were also analyzed by Fourier transformed infrared (FTIR) spectroscopy. As shown in Fig. 2, the O—H bending (1634 cm^{-1}) and O—H stretching (3200–3400 cm^{-1}) signals of water molecules in different electrolytes were collected. With the addition of TEGDME, a slight blue shift of the O—H stretching vibrations was detected, while the symmetric vibration band weakened, implying the formation of H-bond between TEGDME and H_2O [32]. Specifically, the broad O—H stretching vibration can be deconvoluted into three components based on the environments of water molecules: (1) NW (≈3205cm^{-1}): the network water corresponds to the water molecules connected by strong hydrogen bonds; (2) IW (≈3433cm^{-1}): the intermediate water represents the water molecules with distorted hydrogen bonds; and (3) MW (≈3560cm^{-1}): the multimer water belongs to the water molecules standing as free monomers, dimers or trimers in weak connections [33, 34]. As shown in Fig. S1, the introduction of TEGDME in the aqueous Zn $(OTF)_2$ electrolyte disrupted the strong hydrogen bond networks, which the NW proportion decreased from 57.25% in 2mZn to 50.67% in 2mZn-TEGDME, while the IW and MW proportions increased. Raman spectra were collected to further confirm the solvation structure evolution in the electrolytes. In the Raman region of -SO_3 stretching vibrations in OTF anion (Fig. 1c), the broad peak can be divided into 3 parts: free anions (FA, ~1028 cm^{-1}), solvent-separated ion pairs (SSIP, Zn^{2+}–$(solvent)_n$–OTF, ~1033 cm^{-1}), aggregation and contact ion pairs (AGG/CIP, Zn^{2+}–OTF, ~1027 cm^{-1}), respectively [29]. The fraction of aggregation (AGG) and contact ion pairs (CIP) components distinctly increases from 16.9% to 27.9% when TEGDME was introduced, revealing the altered solvation structure with more anions into the inner Zn^{2+}-solvation sheath due to the favorable solvation capability of TEGDME with Zn^{2+}. Such a change would be beneficial to the electrochemical reduction of cation-anion complexes for the formation of robust anion-derived solid-electrolyte interphases (SEI) on the electrodes and contribute to an altered interfacial chemistry, consequently improving the cycling stability and reversibility of electrode materials [35,36].

The ionic conductivities of the electrolytes were also characterized to unveil the impact from the introduced TEGDME as co-solvent. As shown in Fig. 1d, the ionic conductivity of 2mZn-TEGDME (1.26×10^{-2} S cm^{-1}) is calculated to be slightly lower than that of 2mZn electrolyte (2.04×10^{-2} S cm^{-1}), divulging the impairment of ionic transportation caused by the electrolyte structure change [29]. In addition, the wettability of the electrolytes on Zn foils were also performed. The contact angle measurements demonstrate that the 2mZn-TEGDME electrolyte on Zn electrode features lower angles of 50.3° and 51.1°, which are much lower than those of 2mZn counterpart (71.0° and 71.8°, Fig. 1e). The enhanced surface wettability can be attributed to the reduced interfacial free energy on the Zn electrode in the presence of TEGDME, which will facilitate the homogeneous Zn deposition. [37,38].

To evaluate the reversibility of Zn plating/stripping behavior in the electrolytes with TEGDME, symmetric Zn||Zn cells and asymmetric Zn||Cu cells were assembled. Fig. 2a displays the galvanostatic cycling performances of the Zn||Zn cells in different electrolytes at 0.5 mA cm^{-2} and 0.5 mAh cm^{-2} with a fixed plating/stripping time of 1 h. In the TEGDME-containing electrolyte, the cell exhibits ultra-long cycling stability over 4500 h without obvious voltage hysteresis, which is much better than the 2mZn counterpart (about 400 h), while the cell in the 2mZn-TEGDME electrolyte displays larger overpotentials than the baseline electrolyte. Fig. 2b compares the Coulombic efficiencies (CEs) of the asymmetric Zn||Cu cells upon cycling in these two electrolytes, and the corresponding voltage profiles are shown in Fig. 2c and d. The nucleation and plateau overpotentials in the 2mZn-TEGDME electrolyte are higher than those of the blank 2mZn electrolyte, due to the decreased ionic conductivity and increased viscosity in the presence of organic solvent [29,30,39]. The higher nucleation overpotential will facilitate smaller grains during the initial Zn deposition and contribute to more uniform Zn^{2+} deposition [40]. Event thought, the Zn||Cu cell in 2mZn-TEGDME electrolyte exhibits much higher CEs (> 95% in average) and stripping-plating stability over 800 cycles at 0.5 mA cm^{-2}, better than those in 2mZn electrolyte. These results validate the effectiveness of TEGDME additives on improving Zn utilization. In particular, Zn||2mZn-TEGDME||Cu cells display relatively low CEs initially, considering that they might be due to the unstable SEI formed on copper sheet. It is also noted that cells in the 2mZn-TEGDME electrolyte exhibits a larger overpotential (about 200 mV) during Zn platting/stripping, in view of the decreased ionic conductivity by the introduction of organic TEGDME (Fig. 1d). To further unveil the charge transfer behaviors, electrochemical impedance spectroscopy (EIS) investigation was applied on the cells before and after cycling. The Nyquist plots collected on the Zn||Cu cells in these two electrolytes before and after 50 cycles are presented in Fig. 2e and f, and the fitted parameters are listed in

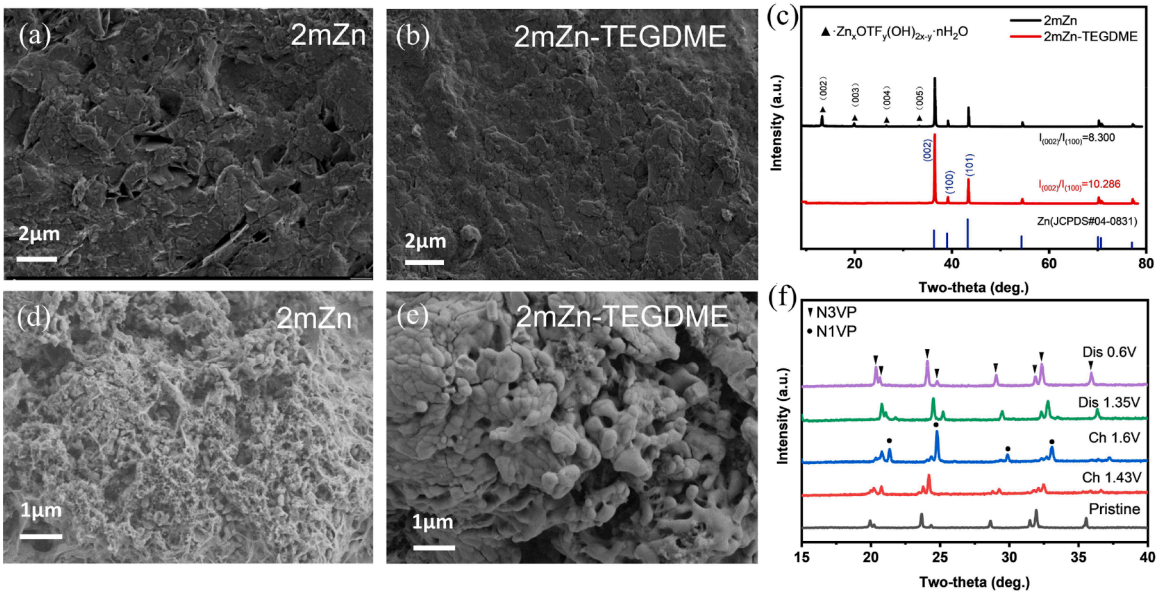

Fig. 4. Morphological analysis and structure evolutions of the cycled electrodes. SEM images of the Zn electrodes (a, b) and NVP cathode (c, d) after 50 cycles (discharged state) in 2mZn and 2mZn-TEGDME electrolytes. (e) XRD patterns of Zn electrode before and after 50 cycles in 2mZn and 2mZn-TEGDME. (f) Ex-situ XRD patterns of the NVP electrodes at different charged and discharged states in 2mZn-TEGDME [N1VP: $NaV_2(PO_4)_3$; N3VP: $Na_3V_2(PO_4)_3$].

Table S1. The impedances of the Zn||Cu cells significantly decrease after cycling, while the cell in TEGDME-containing electrolyte exhibits a lower charge-transfer resistance and then reaches a stable value, suggesting the facilitated charge-transfer kinetics by the introduction of TEGDME co-solvent.

Finally, Zn||NVP full cells were fabricated to investigate the influence of TEGDME additive on the stability of NVP cathode in aqueous electrolyte. The NVP powders were synthesized according to our previous work [26], and the X-ray diffraction (XRD) patterns and scanning electron microscopy (SEM) images were shown in Fig. S1 and S2, illustrating their high purity in crystal phase and typically porous structure constructed by the NVP nanoparticle and carbon frameworks. Fig. 3a and 3b present the typical galvanostatic charge-discharge curves of the cells at 1st and 100th cycles in the two electrolytes at 50 mA g^{-1}. The specific discharge capacity for the 1st cycle of the cell in 2mZn-TEGDME electrolyte is 97 mAh g^{-1}, higher than that in 2mZn electrolyte (80 mAh g^{-1}), which can be attributed to the well suppressed structure degradation and dissolution of NVP active materials in the modified electrolyte during the (de)intercalation of cations (Na^+ and Zn^{2+}), leading to higher reversible capacity [41]. After 100 cycles, the cell in 2mZn suffers from a severe capacity fading (only about 20 mAh g^{-1}), and voltage profile change, resulting from the complete NVP decomposition [26,42]. However, much higher capacity and stable voltage profile curves were observed after 100 cycles in 2mZn-TEGDME electrolyte with a capacity retention of 70.1% after 100 cycles. Even after 370 cycles, a high capacity of 48 mAh g^{-1} was retained within an average CE of 99.3%. Meanwhile, as presented in Fig. 3c, the capacity of the cell dropped rapidly after 50 cycles with a decrease in CEs in 2mZn electrolyte. These results clearly demonstrate the superior stability of Zn||NVP cells in the TEGDME-containing aqueous electrolyte. Moreover, EIS experiments were also performed on the full cells before and after cycling, and the results are displayed in Fig. 3d and e. The charge transfer resistance of Zn||2mZn||NVP cells is slightly lower than that of Zn||2mZn-TEGDME||NVP at initial state (Table S2). After 50 cycles, the cell in 2mZn demonstrates a higher charge transfer resistance than that in 2mZn-TEGDME, indicating the suppressed material degradation of NVP in 2mZn-TEGDME electrolyte. Fig. 3f displays the cyclic voltammetry (CV) profiles of the Zn||2mZn-TEGDME||NVP cell at a scan rate of 0.1 mV s^{-1}. After four cycles from 2nd to 5th, the two pairs of redox peaks are well overlapped, demonstrating the good reversibility. CV tests at various scan rates were also performed to gain insight into the reaction kinetics of NVP (Fig. S4). The redox peaks of the cell in 2mZn-TEGDME are sharper and more intensive, indicating the facilitated redox kinetics, while the voltage polarization is slightly larger than that in 2mZn, due to the low ionic conductivity in the co-solvent electrolyte. These results clearly suggested that the presence of TEGDME cosolvent can well suppress the dissolution of the NVP materials, and thus facilitate the intrinsically sluggish reaction kinetics of NVP cathode for Zn storage.

To assess the influence of TEGDME additive on the electrode structural evolutions upon stripping/plating reactions, SEM images were recorded on the Zn anodes and NVP cathodes cycled in both 2mZn and 2mZn-TEGDME electrolytes for 50 cycles. The morphology structure of the cycled Zn electrodes in 2mZn (Fig. 4a) shows the cliffy nanoflakes and rough surface due to the by-product formation and severe dendrite growth. In contrast, in the TEGDME-containing electrolyte, a relative smooth and dense surface was observed on the Zn electrode as seen in Fig. 4b. The structural evolution of Zn anodes after cycling was further evaluated by X-ray diffraction (XRD) analysis. As seen in Fig. 4c, the distinct characteristic peaks of $Zn_xOTF_y(OH)_{2x-y}\cdot nH_2O$ at 13.3°,19.9°, 26.6°, 30.2° were detected on the Zn electrode after cycling in 2mZn electrolyte [7,43]. However, the Zn electrode cycled in 2mZn-TEGDME after 50 cycles only demonstrates the characteristic peaks of pristine metallic Zn without any impurity peaks observed, illustrating that the presence of TEGDME in aqueous electrolyte efficiently inhibited the hydrogen evolution and side reactions to achieve a high reversibility. In addition, it has been reported that the Zn (002) is more resistant to the formation of dendrite than Zn (100) and Zn (110) [44,45]. In the TEGDME-containing electrolyte, the Zn deposit exhibits a much higher intensity ratio of Zn (002) to Zn (100) than that in baseline electrolyte (10.286 vs. 8.300), which verifies the organic/inorganic hybrid fluorine-rich AEI enables a preferred (002) crystallite orientation for Zn deposition and lateral migration [29,46]. On the cathode side, the SEM images of NVP electrodes after cycling also display different morphological change in these two electrolytes, in which the electrode was severely corroded to form mossy and rough surface without distinct NVP particles resulting from the degradation and dissolution of NVP, as shown in Fig. 4d. In sharp contrast, the NVP cathode cycled in 2mZn-TEGDME show a smooth surface with distinct NVP particles (Fig. 4e). These results identify that the presence of TEGDME additive

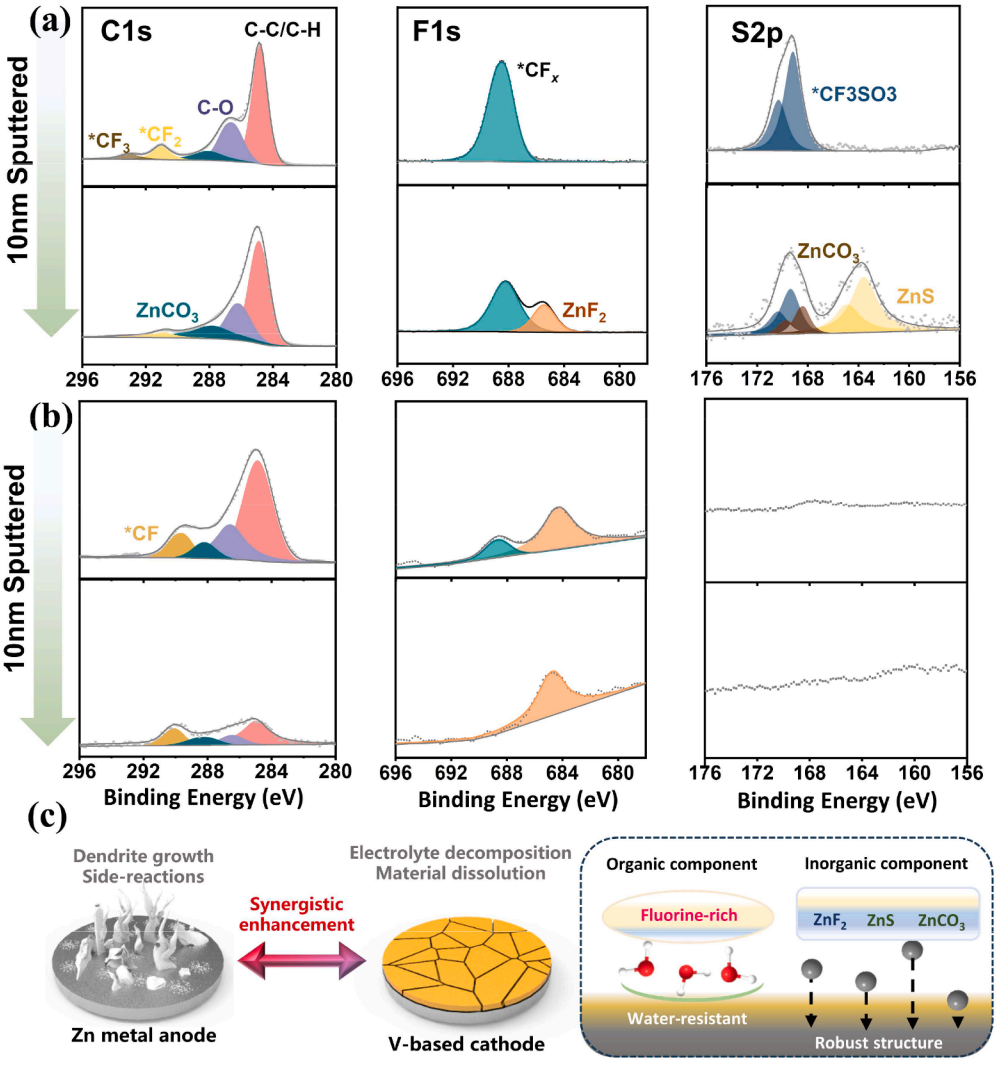

Fig. 5. Characterizations of the interphase layers on the cycled electrodes in 2mZn-TEGDME electrolyte. XPS profiles of C1s, F1s, S2p, Na1s recorded on the (a) NVP cathode and (b) Zn anode before and after Ar^+ sputtering at a depth of 10 nm. (c) Schematic illustration of synergistic enhancement by co-solvent electrolyte.

can not only prevent the Zn anode from by-product formation and dendrite growth, but also help to maintain the structure of NVP and suppress its dissolution, thus improving the long-term cycling stability of the full cells.

Moreover, to further elucidate the structural stability and reversibility of the NVP cathode during operation in 2mZn-TEGDME, ex-situ XRD patterns were collected at different charge and discharge states, as shown in Fig. 4f. When charging from open-circuit voltage (OCV) to 1.6 V, the characteristic peaks of NVP tend to shift to higher 2θ direction along with the appearance of the $NaV_2(PO_4)_3$ (N1VP) phase, due to the extraction of Na^+ from the NVP (i.e., N3VP) structure causing lattice contraction [47]. Upon discharging, the peaks shifted to lower 2θ region and no other impurity peaks were observed at the end of discharging (0.6 V), verifying the reversible (de)intercalation reaction in NVP material [48]. It should be noted that the characteristics peaks of NVP are located at higher 2θ values when discharged to 0.6 V, compared to the pristine NVP electrode, which can be attributed to the co-intercalation of Zn^{2+} cations with smaller ionic radius (0.74 Å) than that of Na^+ (1.02 Å). In addition, the incomplete intercalation of cations will also inevitably lead to the structural shrinkage. These results further reveal that the introduction of TEGDME in aqueous electrolyte can improve the stability of NVP cathode for Zn-metal batteries.

The chemical structure of interphase layers formed on both negative and positive electrodes cycled in 2mZn-TEGDME electrolyte (at discharged states) was further characterized by X-ray photoelectron spectroscopy (XPS) with Ar^+ sputtering. All binding energies were calibrated by using the C1s peak (284.8 eV) as the reference. As shown in Fig. 5a, regarding to the NVP cathode after 10 cycles at fresh state, strong C1s signals are detected, the peaks at 284.8 eV and 286.6 eV are ascribed to the organic components of CC/C—H and C—O species. A small amount of carbonate was detected at 288.2 eV, originating from the decomposition of TEGDME and generation of $ZnCO_3$. Organic -CF_3 (293.0 eV) and -CF_2 (291.1 eV) components are observed, indicating the partial reduction of OTF anions at the NVP electrode surface. Meanwhile, F1s spectra only involve organic *CF_x species, and the S2p peaks illustrate the presence of -SO_3 components, further confirming the organic substances on the top surface. At a depth of 10 nm after sputtering, the intensified peak of O—C = O species suggests the increase of inorganic carbonate content with the removal of outer organic components, which can be also reflected by the O1s spectra (532.4 eV, Fig. S5) [26]. F1s spectra shows the mixture of organic and inorganic species with *CF_x and ZnF_2, and S2p spectra also indicate three major components: -SO_3, $ZnSO_3$ and ZnS, probably resulting in the formation of a thick organic/inorganic inner layer of the cathode-electrolyte interphase (CEI) on NVP. In addition, the signal of O1s spectra also shows the distinct components of C—O/S-O species and $ZnCO_3$ on the cycled NVP electrode, where the content of $ZnCO_3$ increased after sputtering. As demonstrated, it is apparent that the CEI generated in 2mZn-TEGDME

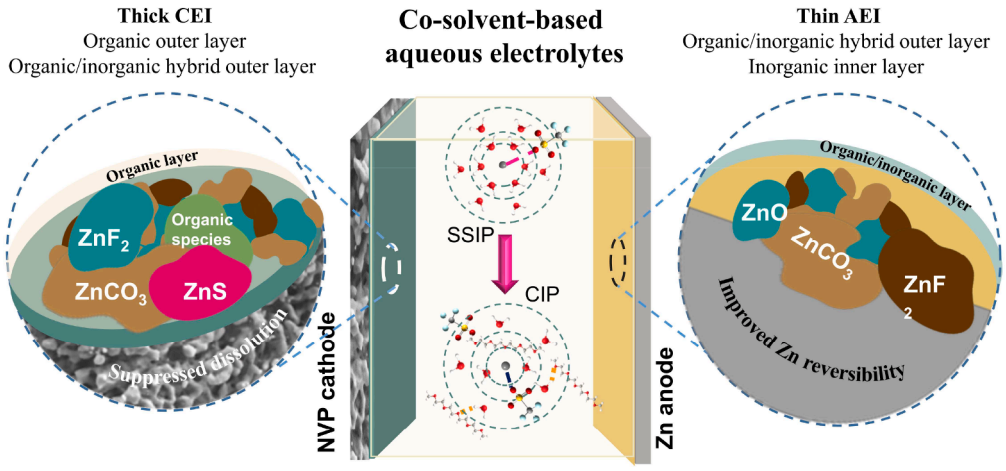

Scheme 1. Illustration of the SEI components induced by co-solvent strategy in aqueous electrolytes for Zn||NVP batteries.

possesses a hybrid structure composed of organic-outer layer and inorganic/organic-inner layer, which can efficiently suppress the water penetration and prevent the dissolution of NVP cathode materials [49, 50].

On the cycled Zn anode, the anode-electrolyte interphase (AEI) is relatively simple, and no sulfur and sodium signals were detected at the top surface and even a depth of 10 nm (Fig. S6). However, C1s spectra evidence the multiple organic components (C—O, C—C, and *CF from the incomplete decomposition of anions) with minor inorganic CO_3^{2-} species. The organic $*CF_x$ and inorganic ZnF_2 species resulting from the decomposition of anions were detected at the top surface. O1s spectra confirm the existence of C—O and CO_3^{2-} species, identifying the outer layer of the AEI is composed of organic/inorganic components. After sputtering within a depth of 10 nm, the C1s and F1s signals become relatively weak in intensity, featuring the low thickness of the AEI. The F1s signal can be only ascribed to the inorganic ZnF_2 fraction. Moreover, the signal of $ZnCO_3$ is reduced while the ZnO signal strengthened after sputtering, indicating an inorganic nature of the inner layer of AEI. These results clearly illustrated that the AEI formed in 2mZn-TEGDME exhibited a rather different architecture to the CEI structure, which consists of an organic/inorganic outer layer and an inorganic inner layer. Such thin and robust inorganic-rich interphase on the Zn electrode features potential Zn^{2+} conduction and corrosion-resistant ability that can effectively suppress the growth of zinc dendrite by inducing lateral Zn^{2+} migration and deposition [51,52]. Note that the Zn species on both topmost surface and deep inner layer were determined, including organic and inorganic components (Fig. S7), which guarantee the Zn^{2+} diffusion in the SEI layers.

Based on the above discussion, the co-solvent and anions can be oxidized on the NVP cathode contributing to a hybrid but thick organic-rich SEI film, while reduced on the Zn metal to form a robust and thin inorganic-rich SEI, synergistically guaranteeing the stability and efficiency of the aqueous Zn||$Na_3V_2(PO_4)_3$ full-cells, as shown in Fig. 5c.

The formation and components of the SEI on both electrodes are schematically shown in Scheme 1. By adding TEGDME as co-solvent, the solvation structure of Zn^{2+} was manipulated, in which the unique TEGDME and OTF co-involved solvation structures can break the H-bond network between water molecules and suppress the side reactions caused by water decomposition. More anions are involved in the solvation sheath of Zn^{2+}, thus prompting the formation of robust solid-electrolyte interphases (SEI) induced by the decomposition of cation-anion complex. The fluorine-rich organic outer layer of CEI efficiently prevent the water molecules contacting the active cathode materials, thus inhibiting the dissolution and structural degradation of NVP cathode. Moreover, thin but robust inorganic-rich AEI can restrain the dendrite growth and relieve the side reactions on the Zn anode to a great extent, which is synergistically contributed to the high reversibility of aqueous Zn batteries.

4. Conclusions

In summary, we have demonstrated a co-solvent electrolyte engineering strategy to induce unique anion-solvation-derived interfacial chemistry in aqueous Zn-metal batteries paired with NASICON-type cathodes. The as-proposed electrolyte formulation enables the formation of a thick and flexible CEI with organic outer layer and inorganic/organic hybrid inner layer architecture, which can efficiently prevent the water penetration and dissolution of cathode materials. In addition, a high-quality thin and robust AEI, composed of an organic/inorganic outer layer and an inorganic inner layer, reinforces the reversibility of Zn anode by suppressing the side reactions and dendrites. Indeed, the Zn anode in the formulated electrolyte exhibits high reversible platting/stripping properties (over 4500 h at 0.5 mA cm ^{2} with 0.5 mAh cm ^{2}). The Zn||NVP cells exhibit a high Coulombic efficiency (around 99.3%) with a capacity retention of 51.5% after 370 cycles. Our findings offer a new understanding of the interfacial chemistries in the co-solvent engineered aqueous electrolyte, and undoubtedly into will give insights into developing highly efficient electrolytes for high performance Zn batteries.

Data availability

Data will be made available on request.

CRediT authorship contribution statement

Chen Hu: Methodology, Formal analysis, Investigation, Writing – original draft. **Gaoli Guo:** Methodology, Formal analysis, Investigation. **Huihua Li:** Investigation, Data curation, Writing – review & editing. **Jian Wang:** Data curation, Writing – review & editing. **Zhengqing Liu:** Resources, Supervision, Data curation. **Leilei Zheng:** Investigation, Data curation. **Huang Zhang:** Resources, Conceptualization, Methodology, Supervision, Writing – review & editing.

Declaration of Competing Interest

The authors declare that they have no known competing financial interests or personal relationships that could have appeared to influence the work reported in this paper.

Acknowledgements

This work was financially supported by the National Natural Science Foundation of China (52377214 and 52307236), the Natural Science Foundation of Chongqing (cstc2020jcyj-msxmX0667), the China Postdoctoral Science Foundation (2023M730885), the Fundamental Research Funds for the Central Universities, and the Helmholtz Association within the Network of Excellence on post-Lithium batteries (ExNet-0035).

References

[1] L.E. Blanc, D. Kundu, L.F. Nazar, Scientific challenges for the implementation of Zn-ion batteries, Joule 4 (4) (2020) 771–799.
[2] N. Zhang, X. Chen, M. Yu, Z. Niu, F. Cheng, J. Chen, Materials chemistry for rechargeable zinc-ion batteries, Chem. Soc. Rev. 49 (13) (2020) 4203–4219.
[3] D.M. Davies, M.G. Verde, O. Mnyshenko, Y.R. Chen, R. Rajeev, Y.S. Meng, G. Elliott, Combined economic and technological evaluation of battery energy storage for grid applications, Nature Energy 4 (1) (2018) 42–50.
[4] G. Zampardi, F.La Mantia, Open challenges and good experimental practices in the research field of aqueous Zn-ion batteries, Nat. Commun. 13 (1) (2022) 687.
[5] Q. Zhao, W. Huang, Z. Luo, L. Liu, Y. Lu, Y. Li, L. Li, J. Hu, H. Ma, J. Chen, High-capacity aqueous zinc batteries using sustainable quinone electrodes, Sci. Adv. 4 (3) (2018) eaao1761.
[6] X. Zeng, J. Mao, J. Hao, J. Liu, S. Liu, Z. Wang, Y. Wang, S. Zhang, T. Zheng, J. Liu, P. Rao, Z. Guo, Electrolyte design for in situ construction of highly Zn^{2+} conductive solid electrolyte interphase to enable high-performance aqueous Zn-ion batteries under practical conditions, Adv. Mater. 33 (11) (2021), 2007416.
[7] L. Zheng, H. Li, X. Wang, Z. Chen, C. Hu, K. Wang, G. Guo, S. Passerini, H. Zhang, Competitive solvation-induced interphases enable highly reversible Zn anodes, ACS Energy Lett. 8 (5) (2023) 2086–2096.
[8] J. Guo, J. Ming, Y. Lei, W. Zhang, C. Xia, Y. Cui, H.N. Alshareef, Artificial solid electrolyte interphase for suppressing surface reactions and cathode dissolution in aqueous zinc ion batteries, ACS Energy Lett. 4 (12) (2019) 2776–2781.
[9] B.F. Cui, X.P. Han, W.B. Hu, Micronanostructured design of dendrite-free zinc anodes and their applications in aqueous zinc-based rechargeable batteries, Small Struct. 2 (6) (2021), 2000128.
[10] Q. Zong, W. Du, C. Liu, H. Yang, Q. Zhang, Z. Zhou, M. Atif, M. Alsalhi, G. Cao, Enhanced reversible zinc ion intercalation in deficient ammonium vanadate for high-performance aqueous zinc-ion battery, Nanomicro Lett. 13 (1) (2021) 116.
[11] C. Zhong, B. Liu, J. Ding, X. Liu, Y. Zhong, Y. Li, C. Sun, X. Han, Y. Deng, N. Zhao, W. Hu, Decoupling electrolytes towards stable and high-energy rechargeable aqueous zinc–manganese dioxide batteries, Nature Energy 5 (6) (2020) 440–449.
[12] Y.X. Li, J.X. Zhao, Q. Hu, T.W. Hao, H. Cao, X.M. Huang, Y. Liu, Y.Y. Zhang, D. M. Lin, Y.X. Tang, Y.Q. Cai, Prussian blue analogs cathodes for aqueous zinc ion batteries, Mater. Today Energy 29 (2022), 101095.
[13] N. Wang, X. Qiu, J. Xu, J. Huang, Y. Cao, Y. Wang, Cathode materials challenge varied with different electrolytes in zinc batteries, ACS Mater. Lett. 4 (1) (2021) 190–204.
[14] Y. Jin, L. Zou, L. Liu, M.H. Engelhard, R.L. Patel, Z. Nie, K.S. Han, Y. Shao, C. Wang, J. Zhu, H. Pan, J. Liu, Joint charge storage for high-rate aqueous zinc-manganese dioxide batteries, Adv. Mater. 31 (29) (2019), 1900567.
[15] F. Wan, X. Wang, S. Bi, Z. Niu, J. Chen, Freestanding reduced graphene oxide/sodium vanadate composite films for flexible aqueous zinc-ion batteries, Sci. China Chem. 62 (5) (2019) 609–615.
[16] F. Wan, X. Zhou, Y. Lu, Z. Niu, J. Chen, Energy storage chemistry in aqueous zinc metal batteries, ACS Energy Lett. 5 (11) (2020) 3569–3590.
[17] X. Dai, F. Wan, L. Zhang, H. Cao, Z. Niu, Freestanding graphene/VO_2 composite films for highly stable aqueous Zn-ion batteries with superior rate performance, Energy Storage Mater. 17 (2019) 143–150.
[18] Z. Jian, Y.S. Hu, X. Ji, W. Chen, NASICON-structured materials for energy storage, Adv. Mater. 29 (20) (2017), 1601925.
[19] G. Li, Z. Yang, Y. Jiang, C. Jin, W. Huang, X. Ding, Y. Huang, Towards polyvalent ion batteries: a zinc-ion battery based on NASICON structured $Na_3V_2(PO_4)_3$, Nano Energy 25 (2016) 211–217.
[20] S. Chen, C. Wu, L. Shen, C. Zhu, Y. Huang, K. Xi, J. Maier, Y. Yu, Challenges and perspectives for NASICON-type electrode materials for advanced sodium-ion batteries, Adv. Mater. 29 (48) (2017), 1700431.
[21] P. Hu, T. Zhu, X. Wang, X. Zhou, X. Wei, X. Yao, W. Luo, C. Shi, K.A. Owusu, L. Zhou, L. Mai, Aqueous Zn//$Zn(CF_3SO_3)_2$//$Na_3V_2(PO_4)_3$ batteries with simultaneous Zn^{2+}/Na^+ intercalation/de-intercalation, Nano Energy 58 (2019) 492–498.
[22] C. Wang, L. Sun, M. Li, L. Zhou, Y. Cheng, X. Ao, X. Zhang, L. Wang, B. Tian, H. J. Fan, Aqueous Zn^{2+}/Na^+ dual-salt batteries with stable discharge voltage and high columbic efficiency by systematic electrolyte regulation, Sci. China Chem. 65 (2) (2021) 399–407.
[23] H. Zhang, X.P. Tan, H.H. Li, S. Passerini, W. Huang, Assessment and progress of polyanionic cathodes in aqueous sodium batteries, Energy Environ. Sci. 14 (11) (2021) 5788–5800.
[24] M. Zhou, Y. Chen, G. Fang, S. Liang, Electrolyte/electrode interfacial electrochemical behaviors and optimization strategies in aqueous zinc-ion batteries, Energy Storage Mater. 45 (2022) 618–646.
[25] J. Yue, L. Lin, L. Jiang, Q. Zhang, Y. Tong, L. Suo, Y.s. Hu, H. Li, X. Huang, L. Chen, Interface concentrated-confinement suppressing cathode dissolution in water-in- salt electrolyte, Adv. Energy Mater. 10 (36) (2020), 2000665.
[26] G. Guo, X. Tan, K. Wang, H. Zhang, High-efficiency and stable Zn-Na3V2(PO4)3 aqueous battery enabled by electrolyte-induced interphasial engineering, ChemSusChem 15 (11) (2022), e202200313.
[27] H. Yan, X. Zhang, Z. Yang, M. Xia, C. Xu, Y. Liu, H. Yu, L. Zhang, J. Shu, Insight into the electrolyte strategies for aqueous zinc ion batteries, Chem. Rev. 452 (2022), 214297.
[28] H. Li, Z. Chen, L. Zheng, J. Wang, H. Adenusi, S. Passerini, H. Zhang, Electrolyte strategies facilitating anion-derived solid-electrolyte interphases for aqueous zinc–metal batteries, Small Methods doi: 10.1002/smtd.202300554.
[29] G. Ma, L. Miao, Y. Dong, W. Yuan, X. Nie, S. Di, Y. Wang, L. Wang, N. Zhang, Reshaping the electrolyte structure and interface chemistry for stable aqueous zinc batteries, Energy Storage Mater. 47 (2022) 203–210.
[30] F. Ming, Y. Zhu, G. Huang, A.H. Emwas, H. Liang, Y. Cui, H.N. Alshareef, Co-solvent electrolyte engineering for stable anode-free zinc metal batteries, J. Am. Chem. Soc. 144 (16) (2022) 7160–7170.
[31] J. Cong, X. Shen, Z. Wen, X. Wang, L. Peng, J. Zeng, J. Zhao, Ultra-stable and highly reversible aqueous zinc metal anodes with high preferred orientation deposition achieved by a polyanionic hydrogel electrolyte, Energy Storage Mater. 35 (2021) 586–594.
[32] Y. Hao, D. Feng, L. Hou, T. Li, Y. Jiao, P. Wu, Gel electrolyte constructing Zn (002) deposition crystal plane toward highly stable Zn anode, Adv. Sci. 9 (7) (2022), 2104832.
[33] L. Ma, T.P. Pollard, Y. Zhang, M.A. Schroeder, M.S. Ding, A.V. Cresce, R. Sun, D. R. Baker, B.A. Helms, E.J. Maginn, C. Wang, O. Borodin, K. Xu, Functionalized phosphonium cations enable zinc metal reversibility in aqueous electrolytes, Angew. Chem. Int. Ed. 60 (22) (2021) 12438–12445.
[34] J.B. Brubach, A. Mermet, A. Filabozzi, A. Gerschel, D. Lairez, M.P. Krafft, P. Roy, Dependence of water dynamics upon confinement size, J. Phys. Chem. B 105 (2) (2001) 430–435.
[35] L. Suo, D. Oh, Y. Lin, Z. Zhuo, O. Borodin, T. Gao, F. Wang, A. Kushima, Z. Wang, H.C. Kim, Y. Qi, W. Yang, F. Pan, J. Li, K. Xu, C. Wang, How solid-electrolyte interphase forms in aqueous electrolytes, J. Am. Chem. Soc. 139 (51) (2017) 18670–18680.
[36] C. Li, R. Kingsbury, L. Zhou, A. Shyamsunder, K.A. Persson, L.F. Nazar, Tuning the solvation structure in aqueous zinc batteries to maximize Zn-ion intercalation and optimize dendrite-free zinc plating, ACS Energy Lett. 7 (1) (2022) 533–540.
[37] J. Hao, L. Yuan, C. Ye, D. Chao, K. Davey, Z. Guo, S.Z. Qiao, Boosting zinc electrode reversibility in aqueous electrolytes by using low-cost antisolvents, Angew. Chem. Int. Ed. 60 (13) (2021) 7366–7375.
[38] G. Ma, S. Di, Y. Wang, W. Yuan, X. Ji, K. Qiu, M. Liu, X. Nie, N. Zhang, Zn metal anodes stabilized by an intrinsically safe, dilute, and hydrous organic electrolyte, Energy Storage Mater. 54 (2023) 276–283.
[39] C. Wu, C. Sun, K. Ren, F. Yang, Y. Du, X. Gu, Q. Wang, C. Lai, 2-methyl imidazole electrolyte additive enabling ultra-stable Zn anode, Chem. Eng. J. 452 (2023), 139465.
[40] J. Dong, H. Dai, Q. Fan, C. Lai, S. Zhang, Grain refining mechanisms: initial levelling stage during nucleation for high-stability lithium anodes, Nano Energy 66 (2019), 104128.
[41] S. Liu, J. Mao, W.K. Pang, J. Vongsvivut, X. Zeng, L. Thomsen, Y. Wang, J. Liu, D. Li, Z. Guo, Tuning the electrolyte solvation structure to suppress cathode dissolution, water reactivity, and Zn dendrite growth in zinc-ion batteries, Adv. Funct. Mater. 31 (38) (2021), 2104281.
[42] W. Li, X. Jing, K. Jiang, D. Wang, Observation of structural decomposition of $Na_3V_2(PO_4)_3$ and $Na_3V_2(PO_4)_2F_3$ as cathodes for aqueous Zn-ion batteries, ACS Appl. Energy Mater. 4 (3) (2021) 2797–2807.
[43] L. Yu, J. Huang, S. Wang, L. Qi, S. Wang, C. Chen, Ionic liquid “water pocket” for stable and environment-adaptable aqueous zinc metal batteries, Adv. Mater. 35 (21) (2023), 2210789.
[44] D. Yuan, J. Zhao, H. Ren, Y. Chen, R. Chua, E.T.J. Jie, Y. Cai, E. Edison, W. Manalastas Jr., M.W. Wong, M. Srinivasan, Anion texturing towards dendrite-free Zn anode for aqueous rechargeable batteries, Angew. Chem. Int. Ed. 60 (13) (2021) 7213–7219.
[45] K.E. Sun, T.K. Hoang, T.N. Doan, Y. Yu, X. Zhu, Y. Tian, P. Chen, Suppression of dendrite formation and corrosion on zinc anode of secondary aqueous batteries, ACS Appl. Mater. Interfaces 9 (11) (2017) 9681–9687.
[46] Y. Lin, Z. Mai, H. Liang, Y. Li, G. Yang, C. Wang, Dendrite-free Zn anode enabled by anionic surfactant-induced horizontal growth for highly-stable aqueous Zn-ion pouch cells, Energy Environ. Sci. 16 (2) (2023) 687–697.
[47] K. Wang, H. Li, G. Guo, L. Zheng, S. Passerini, H. Zhang, Enabling multi-electron reactions in NASICON positive electrodes for aqueous zinc-metal batteries, ACS Energy Lett 8 (4) (2023) 1671–1679.
[48] Z. Jian, C. Yuan, W. Han, X. Lu, L. Gu, X. Xi, Y.S. Hu, H. Li, W. Chen, D. Chen, Y. Ikuhara, L. Chen, Atomic structure and kinetics of NASICON $NaxV_2(PO_4)_3$ cathode for sodium-ion batteries, Adv. Funct. Mater. 24 (27) (2014) 4265–4272.
[49] D. Li, L. Cao, T. Deng, S. Liu, C. Wang, Design of a solid electrolyte interphase for aqueous Zn batteries, Angew. Chem. Int. Ed. 60 (23) (2021) 13035–13041.

[50] Q. Liu, Y. Sun, S. Wang, Q. An, L. Duan, G. Zhao, C. Wang, K. Doyle-Davis, H. Guo, X. Sun, Highly adaptable SEI/CEI interfacial layers enabling remarkable performance of high-nickel solid-state batteries, Mater. Today 64 (2023) 21–30.
[51] L. Ma, Q. Li, Y. Ying, F. Ma, S. Chen, Y. Li, H. Huang, C. Zhi, Toward practical high-areal-capacity aqueous zinc-metal batteries: quantifying hydrogen evolution and a solid-ion conductor for stable zinc anodes, Adv. Mater. 33 (12) (2021), 2007406.
[52] J. Han, H. Euchner, M. Kuenzel, S.M. Hosseini, A. Groß, A. Varzi, S. Passerini, A thin and uniform fluoride-based artificial interphase for the zinc metal anode enabling reversible Zn/MnO_2 batteries, ACS Energy Lett. 6 (9) (2021) 3063–3071.